Siegfried, M.R., et al., 2023, The life and death of a subglacial lake in West Antarctica: Geology,
https://doi.org/10.1130/G50995.1

SUPPLEMENTAL MATERIALS

Supplemental Figures

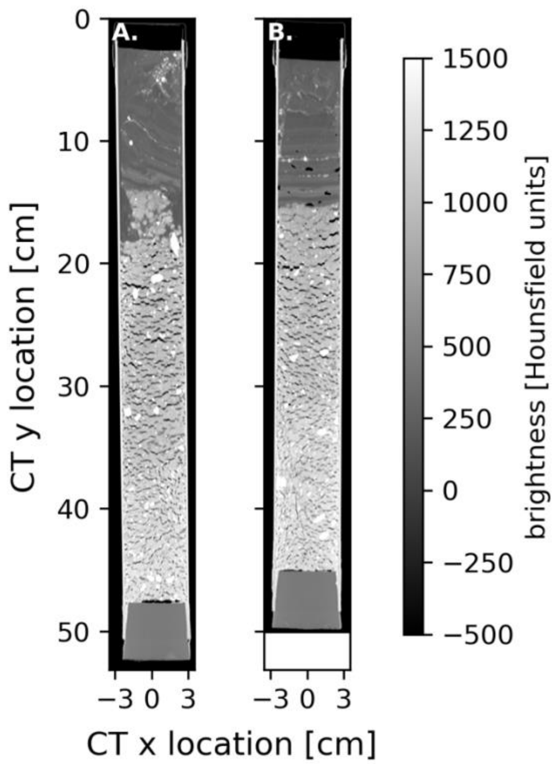

Fig. S1. Computed tomography (CT) imagery from a single vertical slice of (A) core SLM18-01UW-A with deformation of lake sediments that likely occurred during or after retrieval and (B) core SLM18-01UW-C with preserved lake sediment laminations.

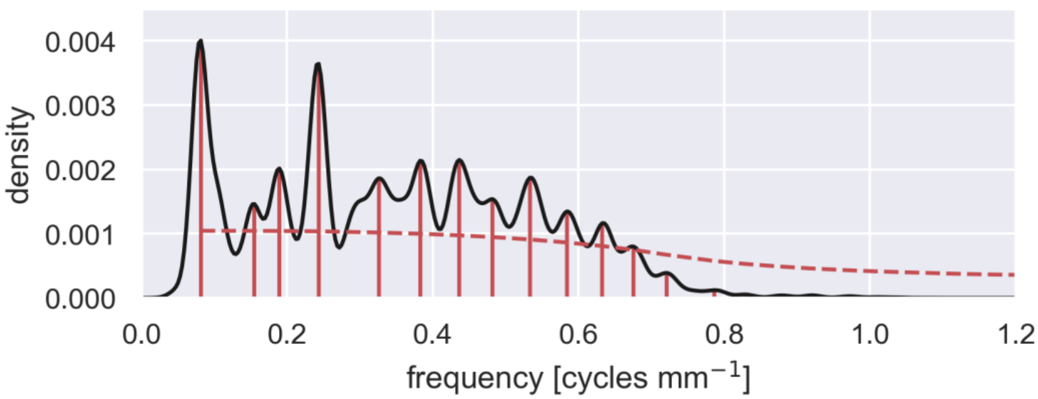

Fig. S2. Kernel density estimate of lamination frequency (in cycles mm^{-1}) estimated using a robust red noise multi-taper method (Meyers, 2012); this kernel density estimate is shown as a violin plot in **Fig. 2A**. Vertical red lines show all peaks identified in the kernel density estimate, with dotted red line indicating the 90% significance level based on f-test statistics. Although the dominant frequencies are at 0.08184 and 0.2438 cycles mm^{-1}, all 12 frequencies that exceeded the 90% significance threshold (**Table S1**) were included in our average spectral misfit analysis.

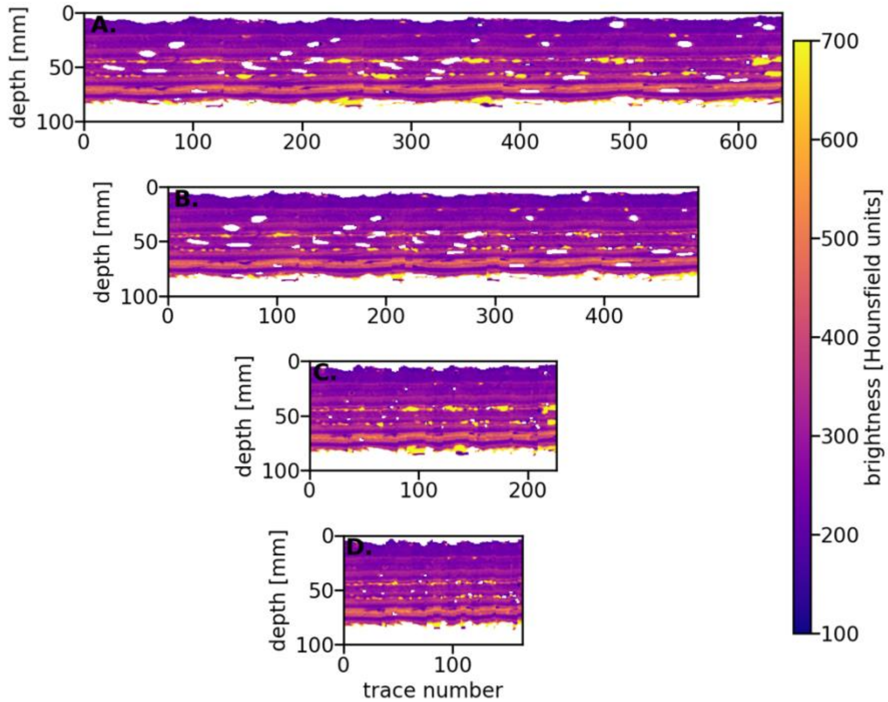

Fig. S3. Computed tomography (CT) imagery used in laminated lake sediment statistical analysis. (**A**) Unfiltered CT image of all 640 traces from the five CT slices with minimal deformation in core SLM-1801-01UW-C. (**B**) 484 traces from five CT slices (panel A) filtered for clasts (identified as brightness values >800). (**C**) 226 traces from five CT slices (panel A) filtered for voids (identified as brightness values <0). (**D**) Final dataset of 164 traces from five CT slices (panel A) filtered for both clasts and voids.

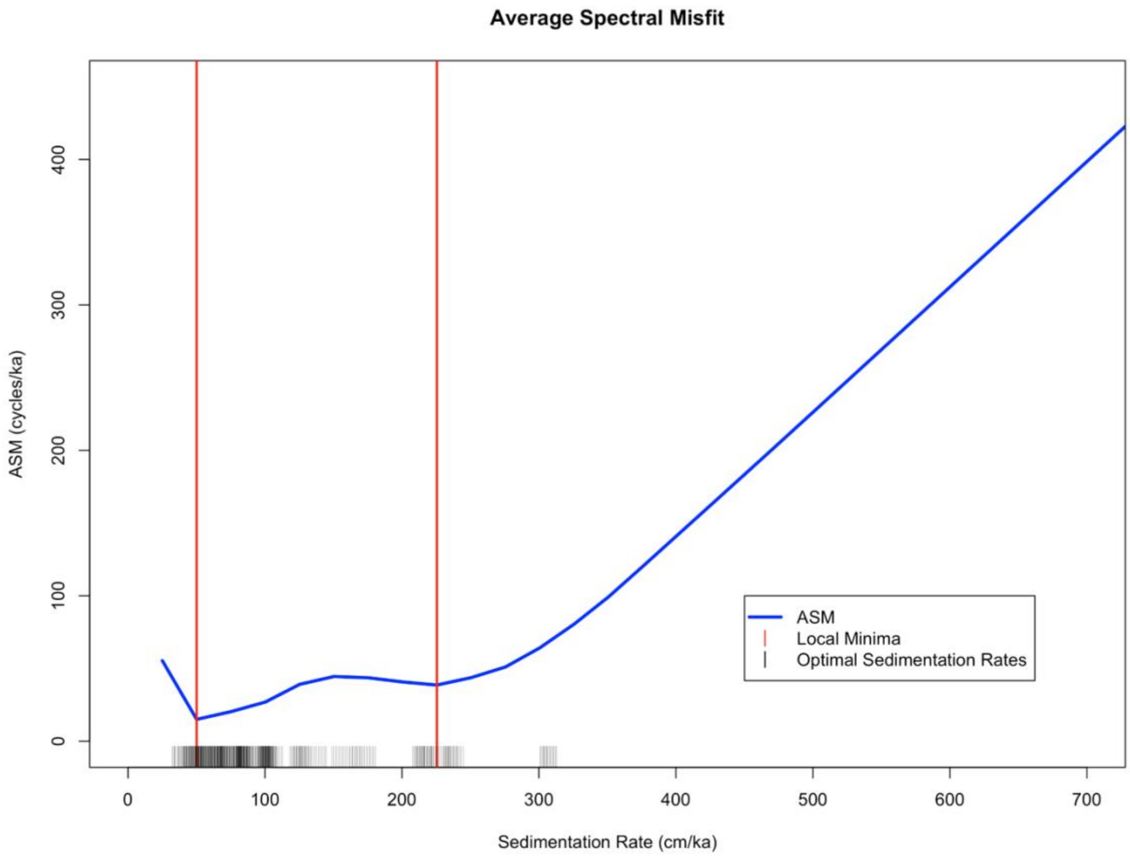

Fig. S4. Average misfit values calculated for all 164 traces over an extended range of sedimentation rates. The majority of optimal sedimentation rates are less than the upper bound of 250 cm ka^{-1} (2.5 mm yr^{-1}).

Supplemental Table

Frequency (cycle mm^{-1})	Period (mm)
0.08184	12.22
0.1557	6.423
0.1898	5.269
0.2438	4.103
0.3261	3.066
0.3829	2.611
0.4369	2.289
0.4824	2.073
0.5335	1.874
0.5846	1.710
0.6329	1.580
0.6755	1.480

Table S1. Lamination frequencies and corresponding periods that exceeded the 90% significance threshold based on our application of a robust red-noise multi-taper method (Meyers, 2012).

Supplemental Methods

Surface height processing

We processed Global Positioning System (GPS) and multi-mission altimetry to generate an extended time series of height at the Mercer Subglacial Lake (SLM) borehole access location (84.640287° S, 149.501340° W) from September 2003 to April 2021 (**Fig. 1B)**. We selected the SLM access site to be at the orbital crossover of Ice, Cloud, and land Elevation Satellite (ICESat) ground tracks 0369 and 1288 in order to provide the most detailed context back to 2003. We interpolated bespoke satellite altimetry-derived digital elevation models (DEMs) to this SLM access location. Processing for each satellite altimetry mission is described below, followed by a description of GPS processing. Each dataset was processed to an ice-surface height estimate with no additional corrections applied.

ICESat Data and Processing: The ICESat mission was a NASA laser altimetry mission that collected data to 86° S from September 2003 to October 2009. Due to laser energy considerations, data collection occurred during 19 laser operational periods that were 12- to 55-days long, spaced at 4–6 months. We downloaded orbital ground tracks 0369 and 1288 of the ICESat GLAH12 data product (GLAS/ICESat L2 Global Antarctic and Greenland Ice Sheet Altimetry Data (HDF5), version 34) from the National Snow and Ice Data Center (Zwally et al., 2014). We subset the data to a box centered on the SLM access site with dimensions 250 m x 250 m [approximately the size the orbital crossover region due to variability in pointing control that resulted in sub-parallel ground tracks with a root mean squared cross-track separation from the reference ground track of up to 111 m (Siegfried et al., 2011)] and applied the detector saturation (Sun et al., 2017) and Gaussian-centroid (Borsa et al., 2014) corrections provided on the data product. We followed Smith et al. (2009) to generate a time series of dynamic height change over a small (<1 km by <1 km) patch of the ice-sheet surface by solving a system of linear equations that accounts for cross-track slope using all available ICESat data. Whereas Smith et al. (2009) used the least squares solution to interpolate data to a reference ground track, we instead used the solution to solve for the height at the SLM access site for each ICESat footprint within the box (N=61). We aggregated height estimates by track for each campaign, resulting in 20 individual height estimates between October 2003 and September 2009, with an uncertainty of 0.2 m to 0.5 m (calculated as the range of 1σ values for height estimates in each aggregation).

CryoSat-2 Data and Processing: The CryoSat-2 mission has collected radar altimetry data with a 369-day near-repeat orbit to 88° S since July 2010. At the time of writing, data were available through the end of May 2021. Our CryoSat-2 processing followed previous methods for interpolating Level 2 CryoSat-2 synthetic aperture radar interferometric (SARIn) mode data (Baseline D) to a point location (Siegfried et al., 2014), with updates based on more recent CryoSat-2 analysis (Siegfried and Fricker, 2018, 2021). In short, we subset CryoSat-2 SARIn data to the SLM region, performed an iterative three-sigma filter over 10 km sub-regions to remove outliers, and generated a monthly 500 m resolution DEM of the ice surface using three months of CryoSat-2 data (nominally one orbital sub-cycle) and continuous curvature splines in tension (T = 0.7) as our gridding method (Smith and Wessel, 1990). There were between 1141 and 2838 individual CyroSat-2 SARIn height retrievals per time window after filtering. We applied a Gaussian filter with a 6-sigma width of 5000 m to each DEM and interpolated to the SLM access coordinate with bicubic splines. The interpolation step is the largest source of error (Siegfried et al., 2014), with accuracy and precision dependent on the local topography and the specific distribution of CryoSat-2 footprints. We used a Monte Carlo approach to estimate uncertainty for the interpolation method at each time step (i.e., each distribution of CryoSat-2 footprints), in which we repeatedly (N=100) sampled 95% of the CryoSat-2 data for each three-month window to generate a DEM and validated the DEM interpolation at the remaining 5% of data points. Across the 129 timesteps (August 2010 to April 2021), we found that interpolation bias ranged from -0.05 to 0.27 m and interpolation precision (1σ) ranged from 2.55 to 2.94 m. However, this approach neglected that the interferometric processing of CryoSat-2 SARIn data explicitly samples the point-of-closest-approach (i.e., topographic highs) within the large [~1.7 km (McMillan et al., 2013)] cross-track radar footprint. When a subglacial lake drains, the ice surface can form a narrow, local depression (e.g., Siegfried and Fricker, 2021), and so there is likely an additional, significant (1+ m) bias for interpolating to the SLM access site (which is located in the central portion of SLM) near low-stand: this issue can readily be identified by the separation between GPS and CryoSat-2 in early 2012 (**Fig. 1B**). We therefore do not use interpolated CryoSat-2 data to assess the total amplitude of height change at the SLM access site between low stand and time of subglacial access as it likely underestimates the magnitude by $O(1)$ m.

ICESat-2 Data and Processing: NASA's ICESat-2 mission is its satellite laser altimetry follow-on to the ICESat mission. ICESat-2 data has collected data to 88° S with 91-day repeat coverage since 14 October 2018. Unlike the single ground-track design of the ICESat mission, the ICESat-2 mission instrument uses an innovative six-track design to increase data density and capture cross-track slopes, wherein one laser beam is split with diffractive optics into three pairs of ground tracks, with ~3.3 km separation between pairs and ~90 m separate within a pair. We used the ICESat-2 Level 3a ATL06 (Land Ice Height), version 004 data product (Smith et al., 2021, p. 06) and followed a similar processing pipeline for interpolating values to the SLM access site as used for CryoSat-2 processing. We subset the ICESat-2 ATL06 data to the SLM region, filtered data based on the ATL06 summary quality flag (*atl06_qual_summary* == 0), and generated monthly DEMs posted at the same monthly interval using three months of ICESat-2 data and continuous curvature splines in tension followed by a Gaussian filter for gridding (Smith and Wessel, 1990). There were between 31,167 to 206,121 ATL06 footprints in each processing window, or one to two orders of magnitude greater density compared to CryoSat-2 SARIn-mode data. We used a finer spatial resolution (250 m) and finer Gaussian filter (6-sigma width of 1750 m) given this increased data density of the ICESat-2 mission compared to that of the CryoSat-2 mission. Interpolation uncertainty is more difficult to quantify given the exact-repeat design of the ICESat-2 mission. However, it is less dependent on footprint distribution as each 90-day time window has approximately the same footprint geometry due to the exact-repeat mission design; a similar Monte Carlo approach at Academy Glacier, East Antarctica, suggested that the single-point interpolation uncertainty is 0.19 m (Siegfried and Fricker, 2021).

GPS Data and Processing: Continuous GPS stations were installed on lower Mercer and Whillans ice streams soon after the initial discovery of interconnected subglacial lakes in the region (Fricker et al., 2007). The array operated through the Whillans Ice Stream Subglacial Access Research Drilling (Tulaczyk et al., 2014) and Subglacial Antarctic Lakes Scientific Access (Priscu et al., 2021) projects as an evolving experiment of up-to 23 stations that operated until the final stations were removed on 26 November 2019. We used data from three GPS stations that were deployed on SLM: (1) LA09, located on SLM 8.1 km downstream of the SLM access site and operated from 25 January 2008 to 26 November 2019; (2) LA12, deployed about 22 m from the SLM access site and operated from 4 January 2012 to 7 January 2014; and (3) LA17, located about 420 m downstream from the SLM access site at time of breakthrough and operated from 12 December 2016 to 26 November 2019. These stations consisted of a Trimble NetRS or NetR9 receiver, a Trimble Zephyr Geodetic or Zephyr Geodetic II antenna mounted on a metal pole with the antenna 0.5 to 3 m above the snow surface, and a large enough power station (1–2 solar panels, 0–2 wind turbines, 4–10 batteries) to collect data through polar night. Battery degradation and instrument failures caused data interruptions ranging from hours to two years (in the case of a storage card failure at LA09).

We processed our 15 s or 30 s rate GPS data kinematically using a precise point positioning (PPP) technique implemented by Natural Resource Canada's online tool Canadian Spatial Reference System-PPP to estimate the epoch-by-epoch geodetic coordinate of the antenna. In order to generate an ice-surface height time series that is consistent with satellite altimetry, we had to correct our geodetic antenna coordinate for the height of the antenna above the snow surface. Therefore, we also processed the GPS data using interferometric reflectometry (e.g., Larson et al., 2009; Siegfried et al., 2017; Shean et al., 2017), which is a method that uses reflected GPS signals to estimate height of the antenna above the snow surface at daily resolution with 0.02 m accuracy and 0.06 m precision (Siegfried et al., 2017). We aggregated our conventionally processed GPS positions into daily height estimates, filtering days that had less than 120 epochs (i.e., 30 minutes of data at 15 s recording). We calculated daily positions as the median to reduce the impact of large outliers that can be caused by power fluctuations during polar winter. Each daily position estimate included between 129 and 5760 individual epochs in the calculation (suggesting sub-mm precision given a typical individual-epoch vertical precision of 0.1 m). We then subtracted daily GPS reflectometry reflector height estimates from the daily position estimates to generate a time series of ice-surface height at the SLM access site (LA12, LA17).

To compare surface-height change to observed lake water column thickness, we needed to estimate the ice-surface height change at the SLM access site between low stand and time of access; although we did have a GPS station recording at the SLM access site during SLM borehole operations, we did not occupy this site with a GPS station when SLM was at low stand. We therefore used the longer, more continuous ice-surface height time series from LA09 and scaled it based on the ratio of height change between LA09 and LA12/LA17 [i.e., $(h_2^{LA12/LA17} - h_1^{LA12/LA17}) / (h_2^{LA09} - h_1^{LA09})$]. To maximize our signal-to-noise ratio, we only calculated height-change ratios when height-change at an individual GPS station (e.g., $h_2^{LA09} - h_1^{LA09}$) exceeded 11 m, which resulted in 1567 scaling ratios with a mean of 1.19 ± 0.02 (1σ). Ice-surface height at LA09 increased from 102.46 m at SLM low stand on 21 Jul. 2014 to 115.02 m on 26 Dec. 2018, when we broke through to SLM, suggesting a scaled height-change at the SLM access site of 14.9 ± 0.3 m.

Lake-averaged time series generation

To generate lake-averaged height-anomaly time series at SLM, Conway Subglacial Lake, and Upper Conway Subglacial Lake (**Fig. 1C**), we applied the method presented in Siegfried et al. (Siegfried and Fricker, 2021) with no adjustments except inclusion of additional data released (through May 2021, resulting in a final time series data point for April 2021).

SLM access and sediment core operations and analysis

During the 2018–2019 Antarctic field season, the SALSA science team employed a clean access, hot-water drill (Priscu et al., 2013; Michaud et al., 2020) to melt a 0.4 m diameter borehole through 1087 m of Mercer Ice Stream to access SLM (Priscu et al., 2021). We determined that the SLM water column was 15 m deep at the time of access, and over the 8.6 days of scientific operations we deployed a multicoring device (UWITEC, Austria) modified for use in a 0.3 m diameter borehole (Tulaczyk et al., 2014; Michaud et al., 2016; Priscu et al., 2021). This device consists of three, 0.6 m long, 0.06 m diameter core barrels designed to collect an intact sediment-water interface (see Hodgson et al. (2016) for images of the coring device); we deployed the UWITEC device at the maximum winch payout speed (50 m min^{-1}) for the final 10 to 15 m before contacting the sediment. We chose two multicores from our first deployment of the UWITEC coring device (Priscu et al., 2021), SLM-1801-01UW-A (0.49 m; **Fig. S1A**) and SLM-1801-01UW-C (0.46 m; **Fig S1B**), to represent the pristine sediment-water interface and shallow sedimentary sequence unobstructed by subsequent sampling efforts. We plugged each of these cores with a rubber stopper at the base and placed them upright for 24 hours in refrigerated (4 °C) storage covered with a loosely fitting cap. Following the settling period, we removed excess water from the core tops using a pipette in an effort to avoid disturbing core top sediments. We secured each core with a foam plug and cap to avoid sediment disturbance during shipment. Because we also used organic carbon in these cores to assess natural-levels of radiocarbon in the SLM system, no additional measures were taken to preserve core-top structures (Venturelli et al., 2021).

Once multicores arrived at OSU-MGR, we measured whole round sediment cores at 1 cm intervals using a GEOTEK Multi-sensor Core Logger, and we used the Toshiba Aquillon 64 Slice at the OSU College of Veterinary Medicine to obtain computed tomography (CT) scans as a first-order, non-destructive core analysis. We captured 35 Digital Imagine and Communications in Medicine (DICOM) files through the 0.06 m core tube in coronal slices with 0.351 mm by 0.351 mm voxels. We processed DICOM files to create high quality, calibrated core slice- and three-dimensional images using the software package pydicom (Mason et al., 2020). Due to the fine-grained, high-water-content nature of the lake sediments, sampling of individual layers with a toothpick (e.g., Leventer et al., 2002) or resin slabbing (e.g., Lamoureux, 1994) was not considered possible without extreme disturbance to the laminations. Given that fragile laminations can now be expected in cores recovered from Antarctic subglacial lakes, we suggest future projects consider additional coring methods (e.g., Veerschuren, 2000), impregnation of sediments with polymers to more easily prepare thin sections (e.g., Lamoureux, 1994; Boës and Fagel, 2005), and/or securing core tops with Zorbitrol gel to avoid disturbance of the sediment-water interface (e.g., Tomkins et al., 2008) in an effort to maximize the potential of preserving these key sedimentological features for higher fidelity analysis. These methods should be implemented in coordination with best practices for limiting carbon contamination (Venturelli et al., 2021) to ensure other cores can be used for paleoglaciological reconstruction (Venturelli et al., 2020).

Statistical core analysis

To investigate the potential range of statistically significant sedimentation rates, we employed techniques that have been specifically developed for rhythmically deposited geological records that do not contain well-resolved radiometric age data (Meyers and Sageman, 2007). More specifically, we performed a series of Monte Carlo simulations on core image data to constrain variability in the spatial and temporal heterogeneity of sedimentation when applying robust red-noise multi-taper (Mann and Lees, 1996) and average spectral misfit (ASM) (Meyers, 2012) analyses to identify significant sedimentation rates and to improve confidence in our estimates of subglacial lake sedimentation patterns. We then used a multi-Gaussian model to estimate the uncertainty of the most frequently identified significant sedimentation rates.

For our analysis, we first extracted vertical traces of CT calibrated brightness values (in dimensionless Hounsfield units [HU], a standardized linear scale that is referenced to air, -1000 HU, and water, 0 HU) through the undeformed portion of the laminated lake sediment package in core SLM-1801-01UW-C. We did not perform analysis on SLM-1801-01UW-A (**Fig. S1A**) as the contact between diamict and lake sediments was not horizontal, indicating non-vertical penetration, undulation of the modern lakebed surface, or deformation after collection. We automatically segmented all CT slices using a *k*-means clustering approach (Achanta et al., 2012) implemented in scikit-image (van der Walt et al., 2014) and masked non-laminated areas of the core. We selected five slices from the middle of the core (at -13 mm (**Fig. S1B**), -11 mm, -9 mm, -7 mm, and -5 mm) that appeared have the least sidewall deformation as a result of the core retrieval process (see **Fig. S3A** to see all slices we used side-by-side). We cropped each slice to the middle 45 mm to exclude any remaining smearing against the core tube and traced the boundary between the upper ~45 mm of laminated sediments that were deformed (likely as a result of core handling in the field) and the intact ~75 mm of laminated lake sediments; we masked the sediment above the traced boundary. After masking, there were 640 vertical CT brightness traces available (**Fig. S3A**). We filtered 156 traces that contained >2% clasts (identified as brightness values >800; **Fig. S3B**) and 414 traces that contained >2% voids (identified as brightness values <0; **Fig. S3C**). After filtering for both clasts and voids, we had 164 brightness traces (**Fig. S3D**), which we used for our statistical analysis.

We randomly subsampled our 164 vertical traces at 90% using 1000 Monte-Carlo simulations in order to increase confidence around significant signal generation. We conducted sensitivity testing of different numbers of Monte Carlo simulations with a series of stepped simulations per transect (500, 1000, 10,000) in order to determine a threshold above which results were convergent and reproducible. We carried out all time-series analysis in Astrochron (Meyers, 2014). Prior to analysis all data sets were interpolated to a median sampling resolution. We used a robust red noise multi-taper method (Meyers, 2012) to estimate power spectra of laminae thickness (**Fig 3A)** and to test for the presence of coherent harmonic components in the data series for each subsampled transect. We extracted laminae thickness frequencies (in cycles mm^{-1}) that satisfied f-test statistics at 90% significance for further ASM analysis (**Fig. S2**).

We applied ASM analysis (Meyers and Sageman, 2007) to statistically determine plausible sedimentation rates using target values based on statistically significant laminae thickness frequencies and subglacial lake cyclicity (with fill/drain cycles of 4-, 5-, or 6-years; **Fig. 1B**). We applied ASM analysis across 200 sedimentation rates from 0 to 2.5 mm a^{-1} (at 0.0125 mm a^{-1} increments) with significance levels for rejection of the null hypothesis (i.e., sedimentation rate not related to fill-drain cycles) determined using 1000 Monte Carlo simulations. We set this range of sedimentation rates based on previously published paleo subglacial lake and sub-ice-shelf environments (e.g., McKay et al., 2009; Smith et al., 2018). We determined statistically significant optimal sedimentation rates using the critical significance level (the inverse of the number of sedimentation rates) (Meyers and Sageman, 2007). As an additional experiment to assess the validity of this assumption, we performed the same ASM analysis using MTM power spectra of each of the 164 parent traces using a large range of sedimentation rates, from 0 mm yr^{-1} to 120 mm yr^{-1} (0 to 12,000 cm kyr^{-1}) (**Fig. S4**). For each parent trace, we retrieved statistically significant frequencies from a Mann and Lees (1996) MTM analysis, and then we performed ASM analysis using this extended range of sedimentation rates. These ASM analysis for the extended range resulted in the optimal sedimentation rates all between 32 and 314 cm ka^{-1}, and the majority of these sedimentation rates were less than the upper bound of 250 cm ka^{-1} (2.5 mm yr^{-1}) that we used in our final analysis. Above the local minimum at 225 cm ka^{-1}, ASM increased roughly linearly.

Finally, we used a five-Gaussian model to quantify the center and standard deviation of the most frequently identified optimal sedimentation rates. Our analysis resulted in a distribution of significant sedimentation rates, with values that converged at 0.49 ± 0.12 mm a^{-1}, 0.68 ± 0.08 mm a^{-1}, 0.83 ± 0.07 mm a^{-1}, 1.04 ± 0.08 mm a^{-1}, and 2.28 ± 0.17 mm a^{-1} (**Fig. 3B**). A sedimentation rate of 0.68 mm a^{-1} was the most densely identified rate of average sedimentation, which we used as the sedimentation rate for considering the relationship between subglacial lake initiation and regional ice dynamics.

Calculation of SLM age

We estimated the age of SLM as a depositional lake by determining the amount of time required for our optimal sedimentation rate to deposit the observed thickness of lake sediments and estimated the uncertainty of our age using a bootstrapping technique that sampled a distribution of lake-sediment thicknesses and sedimentation rates. We generated a lake-sediment package thickness distribution by calculating the thickness in each of the 625 traces we used from the 5 undeformed CT slices. We defined thickness as the distance between the uppermost and lowermost pixel identified as lake sediments using our unsupervised classification scheme. This resulted in an average lake-sediment thickness of 120 ± 2 mm. We then sampled randomly (with replacement) from the distribution of lake-sediment thicknesses (N = 625) and a Gaussian distribution of sedimentation rates (μ = 0.68 mm a^{-1}; σ = 0.08 mm a^{-1}) to generate 10^6 estimates for the age of SLM. Our resulting age was 180 ± 20 years.

SLM surface and borehole geophysics

Our borehole science operations at SLM provided only a snapshot of the physical lake system. To understand the physical setting over a longer time period, we deployed additional geophysical instrumentation: a vertical fiber-optic mooring from the ice surface through the ice and water columns to the bed below and an autonomous phase-sensitive radio-echo sounder (ApRES). Deployment, processing, and analysis of each of these instruments is described below.

Long term fiber-optic mooring: On 5 Jan. 2019, after the conclusion of borehole science operations, we deployed a distributed temperature sensing (DTS) duplexed, multimode fiber-optic cable from the ice surface to the lakebed. We deployed ~ 1121 m of cable through the 1087 m ice column and 15 m water column, unspooling an additional 19 m of cable onto the lake floor. We attached a small stainless-steel anchor to the end of the cable and allowed the cable to freeze into the ice column at the conclusion of our borehole operations. Shipping issues from the cable manufacturer resulted in UV damage to the coating of the unjacketed end of one of fiber strands (channel 1). The increased fragility due to UV damage resulted in severing one fiber channel during field operations; although we successfully spliced the cable in the field, we elected to collect single-ended measurements (channel 2 only) to ensure long-term data collection from our subglacial observatory. Due to instrument data storage limitations on our Sensornet Oryx DTS, we collected 1200 s acquisitions at 29 h intervals from 18 January 2019 until we retrieved the instrument on 26 November 2019. We installed a power station with two solar panels and 10 100 A h batteries to ensure DTS data collection through polar night.

Accurate DTS calibrations require a continuously monitored reference section of cable with a uniform temperature, and we were not able to establish this over the duration of the deployment due to logistical constraints. Based on the raw Raman spectra backscattered data from within the 15 m water column of SLM, however, we estimated differential attenuation rates ($\Delta\alpha$) within the fiber (**Fig. 1E**) (Hausner et al., 2011). In a section of fiber at uniform temperature, the natural log of the ratio of Raman Stokes to Raman anti-Stokes (hereafter referred to as *R*) varies linearly with distance from the instrument at a slope of $\Delta\alpha$. For each 1200 s integration period during the deployment, we calculated $\Delta\alpha$ based on the slope of *R* over the 15 m of cable in the water column. Through 30 April, this calculation returned a consistent and reliable ($p < 0.05$) value of approximately $7.9\pm1.3 \times 10^{-5}$ m^{-1} (mean $\pm$ 1σ), typical values for DTS installations (Hausner et al., 2011). Starting May 2019, and coincident with the switch of SLM from draining to filling, the linear regression became less reliable (i.e., *p* increased) and the 95% confidence interval broadened (**Fig. 1E**), often including zero (indicating that $\Delta\alpha$ cannot be calculated with 95% confidence). It is unlikely that the change in $\Delta\alpha$ resulted from sources related to ice motion, such as inconsistent dragging of the anchor causing transient strain on the fiber, as these signals would likely not align temporally with the change in lake state, nor would it be propagated into the loose-tube fiber-optic cable construction (a design that is specifically to isolate the fiber core from mechanical impingements). Rather, the temperatures in SLM were likely no longer sufficiently uniform to calculate a reliable $\Delta\alpha$. We infer that this non-uniform temperature profile was a result of the filling of SLM.

ApRES surveying: We deployed an ApRES collocated with GPS station LA17 (~420 m from the SLM borehole) to partition surface-height changes between dynamic ice thickness change from changing basal tractions (e.g., Sergienko et al., 2007) and water-column thickness change from subglacial lake activity. The ApRES instrument is a frequency-modulated continuous wave radar with 200 MHz bandwidth and 300 MHz center frequency, originally designed for measuring vertical strain and sub-ice-shelf melt rates (Brennan et al., 2014; Nicholls et al., 2015). ApRES is phase-coherent, and so data from this instrument can be processed with sub-range-resolution precision by analyzing changes in the phase component of the signal using a Vernier-like process (Brennan et al., 2014). We installed our ApRES system for long-term autonomous data collection on 18 Jan. 2019 with a power station that allowed continuous data until retrieval on 26 Nov. 2019. We processed the ApRES data by determining a coarse ice-thickness based on the range delay and a relative ice permittivity of 3.18, then unwrapped the phase for fine-scale range estimates (Brennan et al., 2014). The resulting ice thickness estimate was not corrected for firn effects.

References

Achanta, R., Shaji, A., Smith, K., Lucchi, A., Fua, P., and Süsstrunk, S., 2012, SLIC Superpixels Compared to State-of-the-Art Superpixel Methods: IEEE Transactions on Pattern Analysis and Machine Intelligence, v. 34, p. 2274–2282, doi:10.1109/TPAMI.2012.120.

Boës, X., and Fagel, N., 2005, Impregnation method for detecting annual laminations in sediment cores: An overview: Sedimentary Geology, v. 179, p. 185–194, doi:10.1016/j.sedgeo.2005.05.001.

Borsa, A.A., Moholdt, G., Fricker, H.A., and Brunt, K.M., 2014, A range correction for ICESat and its potential impact on ice-sheet mass balance studies: The Cryosphere, v. 8, p. 345–357, doi:10.5194/tc-8-345-2014.

Brennan, P.V., Lok, L.B., Nicholls, K., and Corr, H., 2014, Phase-sensitive FMCW radar system for high-precision Antarctic ice shelf profile monitoring: IET Radar, Sonar & Navigation, v. 8, p. 776–786, doi:10.1049/iet-rsn.2013.0053.

Fricker, H.A., Scambos, T., Bindschadler, R., and Padman, L., 2007, An Active Subglacial Water System in West Antarctica Mapped from Space: Science, v. 315, p. 1544–1548, doi:10.1126/science.1136897.

Hausner, M.B., Suárez, F., Glander, K.E., Giesen, N. van de, Selker, J.S., and Tyler, S.W., 2011, Calibrating Single-Ended Fiber-Optic Raman Spectra Distributed Temperature Sensing Data: Sensors, v. 11, p. 10859–10879, doi:10.3390/s111110859.

Hodgson, D.A. et al., 2016, Technologies for retrieving sediment cores in Antarctic subglacial settings: Philosophical Transactions of the Royal Society A: Mathematical, Physical and Engineering Sciences, v. 374, p. 20150056, doi:10.1098/rsta.2015.0056.

Lamoureux, S.F., 1994, Embedding unfrozen lake sediments for thin section preparation: Journal of Paleolimnology, v. 10, p. 141–146, doi:10.1007/BF00682510.

Larson, K.M., Gutmann, E.D., Zavorotny, V.U., Braun, J.J., Williams, M.W., and Nievinski, F.G., 2009, Can we measure snow depth with GPS receivers? Geophysical Research Letters, v. 36, p. L17502, doi:10.1029/2009GL039430.

Leventer, A., Domack, E., Barkoukis, A., McAndrews, B., and Murray, J., 2002, Laminations from the Palmer Deep: A diatom-based interpretation: Paleoceanography, v. 17, doi:10.1029/2001PA000624.

Mann, M.E., and Lees, J.M., 1996, Robust estimation of background noise and signal detection in climatic time series: Climatic Change, v. 33, p. 409–445, doi:10.1007/BF00142586.

Mason, D. et al., 2020, pydicom/pydicom: pydicom 2.1.2:, doi:10.5281/ZENODO.4313150.

McKay, R. et al., 2009, The stratigraphic signature of the late Cenozoic Antarctic Ice Sheets in the Ross Embayment: Geological Society of America Bulletin, v. 121, p. 1537–1561, doi:10.1130/B26540.1.

McMillan, M., Corr, H., Shepherd, A., Ridout, A., Laxon, S., and Cullen, R., 2013, Three-dimensional mapping by CryoSat-2 of subglacial lake volume changes: 3D MAPPING BY CryoSat-2: Geophysical Research Letters, v. 40, p. 4321–4327, doi:10.1002/grl.50689.

Meyers, S.R., 2014, astrochron: An R Package for Astrochronology:, https://cran.r-project.org/package=astrochron.

Meyers, S.R., 2012, Seeing red in cyclic stratigraphy: Spectral noise estimation for astrochronology: Paleoceanography, v. 27, p. PA3228, doi:10.1029/2012PA002307.

Meyers, S.R., and Sageman, B.B., 2007, Quantification of deep-time orbital forcing by average spectral misfit: American Journal of Science, v. 307, p. 773–792, doi:10.2475/05.2007.01.

Michaud, A.B., Skidmore, M.L., Mitchell, A.C., Vick-Majors, T.J., Barbante, C., Turetta, C., VanGelder, W., and Priscu, J.C., 2016, Solute sources and geochemical processes in Subglacial Lake Whillans, West Antarctica: Geology, v. 44, p. 347–350, doi:10.1130/G37639.1.

Michaud, A.B., Vick-Majors, T.J., Achberger, A.M., Skidmore, M.L., Christner, B.C., Tranter, M., and Priscu, J.C., 2020, Environmentally clean access to Antarctic subglacial aquatic environments: Antarctic Science, v. 32, p. 329–340, doi:10.1017/S0954102020000231.

Nicholls, K.W., Corr, H.F.J., Stewart, C.L., Lok, L.B., Brennan, P.V., and Vaughan, D.G., 2015, A ground-based radar for measuring vertical strain rates and time-varying basal melt rates in ice sheets and shelves: Journal of Glaciology, v. 61, p. 1079–1087, doi:10.3189/2015JoG15J073.

Priscu, J.C. et al., 2013, A microbiologically clean strategy for access to the Whillans Ice Stream subglacial environment: Antarctic Science, v. 25, p. 637–647, doi:10.1017/S0954102013000035.

Priscu, J.C. et al., 2021, Scientific access into Mercer Subglacial Lake: scientific objectives, drilling operations and initial observations: Annals of Glaciology, p. 1–13, doi:10.1017/aog.2021.10.

Sergienko, O.V., MacAyeal, D.R., and Bindschadler, R.A., 2007, Causes of sudden, short-term changes in ice-stream surface elevation: Geophysical Research Letters, v. 34, p. L22503, doi:10.1029/2007GL031775.

Shean, D.E., Christianson, K., Larson, K.M., Ligtenberg, S.R.M., Joughin, I.R., Smith, B.E., Stevens, C.M., Bushuk, M., and Holland, D.M., 2017, GPS-derived estimates of surface mass balance and ocean-induced basal melt for Pine Island Glacier ice shelf, Antarctica: The Cryosphere, v. 11, p. 2655–2674, doi:10.5194/tc-11-2655-2017.

Siegfried, M.R., and Fricker, H.A., 2021, Illuminating Active Subglacial Lake Processes With ICESat-2 Laser Altimetry: Geophysical Research Letters, v. 48, p. e2020GL091089, doi:10.1029/2020GL091089.

Siegfried, M.R., and Fricker, H.A., 2018, Thirteen years of subglacial lake activity in Antarctica from multi-mission satellite altimetry: Annals of Glaciology, v. 59, p. 42–55, doi:10.1017/aog.2017.36.

Siegfried, M.R., Fricker, H.A., Roberts, M., Scambos, T.A., and Tulaczyk, S., 2014, A decade of West Antarctic subglacial lake interactions from combined ICESat and CryoSat-2 altimetry: Geophysical Research Letters, v. 41, p. 891–898, doi:10.1002/2013GL058616.

Siegfried, M.R., Hawley, R.L., and Burkhart, J.F., 2011, High-Resolution Ground-Based GPS Measurements Show Intercampaign Bias in ICESat Elevation Data Near Summit, Greenland: IEEE Transactions on Geoscience and Remote Sensing, v. 49, p. 3393–3400, doi:10.1109/TGRS.2011.2127483.

Siegfried, M.R., Medley, B., Larson, K.M., Fricker, H.A., and Tulaczyk, S., 2017, Snow accumulation variability on a West Antarctic ice stream observed with GPS reflectometry, 2007–2017: Geophysical Research Letters, v. 44, p. 7808–7816, doi:10.1002/2017GL074039.

Smith, B., Fricker, H.A., Gardner, A., Siegfried, M.R., Adusumilli, S., Csatho, B.M., Holschuh, N., Nilsson, J., Paolo, F.S., and the ICESat-2 Science Team, 2021, ATLAS/ICESat-2 L3A Land Ice Height, version 4:, doi:10.5067/ATLAS/ATL06.004.

Smith, B.E., Fricker, H.A., Joughin, I.R., and Tulaczyk, S., 2009, An inventory of active subglacial lakes in Antarctica detected by ICESat (2003–2008): Journal of Glaciology, v. 55, p. 573–595, doi:10.3189/002214309789470879.

Smith, W.H.F., and Wessel, P., 1990, Gridding with continuous curvature splines in tension: Geophysics, v. 55, p. 293–305, doi:10.1190/1.1442837.

Smith, A.M., Woodward, J., Ross, N., Bentley, M.J., Hodgson, D.A., Siegert, M.J., and King, E.C., 2018, Evidence for the long-term sedimentary environment in an Antarctic subglacial lake: Earth and Planetary Science Letters, v. 504, p. 139–151, doi:10.1016/j.epsl.2018.10.011.

Sun, X., Abshire, J.B., Borsa, A.A., Fricker, H.A., Yi, D., DiMarzio, J.P., Paolo, F.S., Brunt, K.M., Harding, D.J., and Neumann, G.A., 2017, ICESAT/GLAS Altimetry Measurements: Received Signal Dynamic Range and Saturation Correction: IEEE Transactions on Geoscience and Remote Sensing, v. 55, p. 5440–5454, doi:10.1109/TGRS.2017.2702126.

Tomkins, J.D., Antoniades, D., Lamoureux, S.F., and Vincent, W.F., 2008, A simple and effective method for preserving the sediment–water interface of sediment cores during transport: Journal of Paleolimnology, v. 40, p. 577–582, doi:10.1007/s10933-007-9175-1.

Tulaczyk, S. et al., 2014, WISSARD at Subglacial Lake Whillans, West Antarctica: scientific operations and initial observations: Annals of Glaciology, v. 55, p. 51–58, doi:10.3189/2014AoG65A009.

Veerschuren, D., 2000, Freeze coring soft sediments in tropical lakes: Journal of Paleolimnology, v. 24, p. 361–365, doi:10.1023/A:1008191418497.

Venturelli, R.A. et al., 2021, A framework for transdisciplinary radiocarbon research: use of natural-level and elevated-level ^{14}C in Antarctic field research: Radiocarbon, v. 63, p. 1555–1568, doi:10.1017/RDC.2021.55.

Venturelli, R.A., Siegfried, M.R., Roush, K.A., Li, W., Burnett, J., Zook, R., Fricker, H.A., Priscu, J.C., Leventer, A., and Rosenheim, B.E., 2020, Mid-Holocene Grounding Line Retreat and Readvance at Whillans Ice Stream, West Antarctica: Geophysical Research Letters, v. 47, doi:10.1029/2020GL088476.

van der Walt, S., Schönberger, J.L., Nunez-Iglesias, J., Boulogne, F., Warner, J.D., Yager, N., Gouillart, E., and Yu, T., 2014, scikit-image: image processing in Python: PeerJ, v. 2, p. e453, doi:10.7717/peerj.453.

Zwally, H.J., Schutz, R., Hancock, D., and Dimarzio, J., 2014, GLAS/ICESat L2 Global Antarctic and Greenland Ice Sheet Altimetry Data (HDF5), version 34:, doi:10.5067/ICESAT/GLAS/DATA209.